Cobalt Hexacyanoferrate: Compound Stoichiometry, Infrared Spectroelectrochemistry, and Photoinduced Electron Transfer

Reynaldo O. Lezna*,† and Roberto Romagnoli‡

INIFTA, CONICET-Universidad Nacional de La Plata, CC. 16, Suc. 4, La Plata, Argentina and CIDEPINT, Centro de Investigación y Desarrollo en Tecnología de Pinturas, (1900) La Plata, Argentina

Norma R. de Tacconi§ and Krishnan Rajeshwar§

Department of Chemistry and Biochemistry, The University of Texas at Arlington, Arlington, Texas 76019-0065

Received: October 30, 2001; In Final Form: January 17, 2002

The cobalt hexacyanoferrate system, $M_hCo_k^A[Fe^B(CN)_6]_l$, (where M is an alkali metal cation, and the subscripts *h*, *k*, and *l* are stoichiometric coefficients, and A and B are the formal oxidation states of the Co and Fe metal sites in the structure) was shown to contain a rich series of compounds that are inter-linked through various redox processes (involving both electron and cation transfer) either in the dark or under the near-infrared (IR) activation. These processes were studied by a combined use of cyclic voltammetry, in situ IR spectroelectrochemistry (using both intensity or potential modulation), and ex situ X-ray photoelectron spectroscopy.

Introduction

The electrochemistry of Prussian blue and related metal hexacyanoferrates (MHCF) has been intensely studied in recent years (see refs 1−3 for reviews). Cobalt hexacyanoferrate (CoHCF) is of particular interest from both fundamental and practical perspectives: (a) Both cobalt and iron exist in two common oxidation states (II, III) leading to a multitude of compound stoichiometries and redox situations. (b) CoHCF has unique electrochromic properties with color changes not only dependent on the oxidation states of the Co and Fe redox centers, but also on the nature of the co-cation imbibed by the compound during electroreduction.[4] (c) CoHCF exhibits the phenomenon of reversible photoinduced magnetization.[5−7] (d) The ability of CoHCF to bind electrolyte cations can be exploited in environmental remediation scenarios as exemplified by the separation and transfer of Cs^+ from high sodium waters.[8] (e) CoHCF-modified electrodes have shown good electrocatalytic activity toward a variety of substrates including ascorbic acid, nitrite, hydrazine, *p*-chlorophenol, and hydroxylamine.[9−11] And (f) CoHCF, in addition to its electrochromic properties, also exhibits reversible thermochromism in the 25−85 °C temperature range.[4a,12]

Despite this extensive body of prior electrochemical work, a comprehensive study of the many possible compound stoichiometries in the CoHCF system as a whole (see feature a in the introductory paragraph above), is currently lacking. In this paper, we explore, using a combination of voltammetry, infrared (IR) spectroelectrochemistry, and X-ray photoelectron spectroscopy (XPS), how the CoHCF compound stoichiometry: (a) depends on the preparative history of the film; (b) evolves with the applied potential; and (c) dictates electron and ion transport between the film and the contacting electrolyte either in the dark or under photoexcitation.

* To whom correspondence should be addressed. E-mail: *rolezna@inifta.unlp.edu.ar*

† INIFTA, CONICET-Universidad Nacional de La Plata.

‡ CIDEPINT, Centro de Investigación y Desarrollo en Tecnología de Pinturas.

§ Department of Chemistry and Biochemistry, The University of Texas at Arlington.

Experimental Section

The working electrode was a polycrystalline gold disk from Johnson & Matthey (99.99%). The electrode diameter was 6 mm for voltammetry and 11 mm for in situ IR spectroelectrochemical experiments. A platinum mesh, separated from the main compartment by a porous disk, was used as a counter electrode. Prior to each experiment and just before the electrode was dipped into the solution, a fresh surface was generated by polishing it to a mirror finish with alumina particles down to 0.05 μm followed by rinsing with Millipore Milli-Q water and sonication. Solutions for film growth were prepared with analytical grade reagents 1×10^{-3} M $K_3[Fe(CN)_6] + 1 \times 10^{-3}$ M $Co(NO_3)_2$ mixed in deoxygenated 1M KNO_3. Voltammetry and IR spectroelectrochemistry were performed in 1M KNO_3. Potentials were measured and are quoted against a saturated calomel electrode (SCE) placed in a separate chamber and connected to the cell via a Luggin capillary. Dioxygen was removed by bubbling purified N_2 for at least 30 min.

Infrared spectra were obtained in the 2250−2000 cm^{-1} range. The IR spectroelectrochemical cell was custom-designed with the aim of minimizing radiation losses by solvent (water) absorption. Therefore, the gold electrode was tightly placed flat against an optical window (CaF_2) so as to create a μm thin solution layer. A high throughput dispersive IR spectrometer was used with optics routing the radiation to the electrode at an angle of 60° through the CaF_2 window. The IR light intensity was chopper-modulated at 80 Hz, whereas the potential was either set at a fixed value or left at open circuit. The ensuing changes in the reflected intensity, *R*, were p-polarized and sensed by a narrow-band, high-sensitivity, mercury cadmium telluride detector. The output was rectified by a lock-in amplifier, the final spectrum being, unless stated otherwise, the normalized difference between the optical response at a given potential and that at a potential taken as reference, R_{ref}; i.e., $R/R_{ref} = (R - R_{ref})/R_{ref}$.

The reflected IR intensity was also modulated by applying a square wave potential to the electrode, typically at 11 Hz. The resultant AC signal was then processed in a similar way to that

10.1021/jp013991r CCC: $22.00
Published on Web 03/12/2002

TABLE 1: Compound Stoichiometries and Infrared Cyanide Stretch Frequencies in the CoHCF System

oxidation state of the Fe and Co sites	compound	element ratio			cyanide stretch frequency in Fe−CN−Co bridge (cm^{-1})[a]
		Co/Fe	M/Fe	M/Co	
Fe(II), Co(II)	$Co_2[Fe(CN)_6]$[b]	2	0	0	2080
Fe(II), Co(II)	$M_2\ Co[Fe(CN)_6]$[c]	1	2	2	2085
Fe(II), Co(II)	$M_{1.4}Co_{1.3}\ [Fe(CN)_6]$	1.3	1.4	1.1	2085
Fe(II), Co(II)	$M_2Co_3[Fe(CN)_6]_2$[c]	1.5	1	0.7	2100−2105
Fe(III), Co(II)	$Co_3[Fe(CN)_6]_2$[c]	1.5	0	0	2156
Fe(II), Co(III)	$MCo[Fe(CN)_6]$	1	1	1	2125
Fe(II), Co(III), Co(II)	$M_{0.4}Co_1IIICo_{0.3}\ II[Fe(CN)_6]$	1.3	0.4	1.1	2120−2130
Fe(III), Co(III)	$Co[Fe(CN)_6]$	1	0	0	2190−2200

[a] IR data from refs 15c, 15d, 7a, 19−22. [b] Not electrochemically relevant; see text. [c] Implicated in previous electrochemical studies; see text.

of intensity modulation (see above). The two types of IR modulation spectroscopy techniques have been described in detail elsewhere.[15,16]

X-ray photoelectron spectra (XPS) of CoHCF films were obtained with a Physical Electronics Model 5000C system fitted with an aluminum anode (1486.6 eV) as described elsewhere.[17] Photoinduced activation experiments utilized a conventional single compartment cell fitted with a quartz window. Potentials were applied using a VoltaLab 80 Universal Electrochemical Laboratory (Radiometer Analytical S. A., Villeurbanne, France). A 100 W quartz halogen lamp (Oriel) through a cutoff filter ($\lambda > 675$ nm) was used as light source. The incident light flux was 2.1 mW/cm^2.

Films of variable CoHCF loadings were grown on Au electrodes by three methods, namely: (a) potentiodynamic cycling on gold substrate, (b) coagulation plus potentiodynamic cycling, and (c) potentiodynamic cycling starting with the gold substrate at 1.2 V, that is, covered with an oxide layer (see below).

Thin films (5 mC/cm^2) were grown (procedure a above) by introducing the Au electrode in the reactant solution followed immediately by 30 potential cycles at 50 mV/s, without a waiting period for coagulation. These films had a nominal CoHCF loading of 5.2×10^{-8} mol/cm^2 as assessed from the Faradaic redox charge corresponding to [Co(II),Fe(II)] ⇔ [Co(II),Fe(III)] and [Co(II),Fe(II)] ⇔ [Co(III),Fe(II)] processes. These are referred to as thin films as their thickness estimated with 10.4 Å as the unit cell length[18] is in the 80−85 nm range.

For procedure "b" above, the reactants, 1×10^{-3}M $K_3[Fe(CN)_6] + 1 \times 10^{-3}$M $Co(NO_3)_2$, were mixed in deoxygenated 1M KNO_3, by adding an aqueous solution of $Co(NO_3)_2$ to a nitrogen-stirred aqueous ferricyanide solution. During the electrochemical cycling, the initially clear reactant solution evolved to a suspension because of the chemical reaction of hexaaquocobalt species, $[Co(H_2O)_6]^{2+}$, with $[Fe(CN)_6]^{3-}$. The film was *initially* formed at open circuit for 20 min. The electrode was then potentiodynamically cycled between 0.0 and 0.95 V (30 cycles) at 50 mV s^{-1}.

Coagulation can be prevented from taking place on the Au surface at the reactant mixing/work up stage (procedure c above). To this end, the Au electrode once dipped in the solution, was kept poised at 1.2 V so that the oxide layer formed in situ protects the surface until the potentiodynamic cycles are initiated.

Results and Discussion

CoHCF Compound Stoichiometries and Their Inter-Relationships. Before presenting and discussing our data, it is instructive to examine the various compounds that can exist (or have been reported) in the CoHCF system and their redox (and structural) connectivities. The end compounds bear Co:Fe stoichiometries of 2.0 and 1.0 respectively as represented by the members, $Co^{II}_2[Fe^{II}(CN)_6]$ and $Co^{III}[Fe^{III}(CN)_6]$ (Table 1). However, the 2:1 compound cannot undergo redox reactions without losing Co sites from the structure. Thus, within the framework of this study, only compounds in the range of Co/Fe ratios from 1.5 to 1.0 are pertinent (see below).

In the $Co^{II}_3[Fe^{III}(CN)_6]_2$ structure, not all the cobalt ions are octahedrally coordinated via CN bridges to iron ions because there are one-third of $[Fe(CN)_6]^{3-}$ species less than the required amount. At the $[Fe(CN)_6]^{3-}$ vacancies, cobalt is bonded to water molecules, resulting, on the average, in one cobalt bonded to four nitrogens (from cyanide) and two oxygens (from water). It is the range of compounds with Co/Fe ratios between 1.5 and 1.0 that makes the CoHCF system interesting from both fundamental and practical perspectives (see Introduction above).

When the cobalt or the iron sites undergo reduction (from their III oxidation state), cations have to move into the CoHCF structure to maintain electroneutrality. Several of these compounds are shown in Table 1. These co-cations are usually alkali metals and they occupy tetrahedral sites in the CoHCF network.[23−25] In the $M^ICo^{II}[Fe^{III}(CN)_6]$ structure (M = co-cation) for example, each cobalt is bonded to six nitrogens and the "foreign" co-cations are located in half of the available tetrehedral lattice sites in a perfect face centered cubic (fcc) structure.[23−25]

In intermediate cases, the divalent Co ion occupies all the fcc sites, whereas occupation of the octahedral sites by $[Fe(CN)_6]^{3-}$ varies from 67 to 100% as a function of the amount of alkali metal cation in the structure. This range of compounds may be represented by $M^I_{3y-8}Co^{II}_4[Fe^{II}(CN)_6]_y$.[7a] To complicate matters even further, the Co species may exist in mixed II, III oxidation states within the structure. Thus, in the structure $M_{0.4}Co_{1.3}[Fe(CN)_6]$ (Table 1), there are Co(III) and Co(II) species in a 3:1 ratio. These Co species are also in different coordination environments with $^3/_4$ of the Co(III) ions being bonded to four nitrogens and two oxygens (from water molecules), the remaining $^1/_4$ of the Co(II) ions being saturatively six-coordinated to nitrogens.[7a] This set of compounds are closely related to the CoHCF structures displaying photoinduced magnetization.[5]

Which of the above CoHCF species have been reported in the electrochemical literature prior to this study? To our knowledge, only the $M^ICo^{II}[Fe^{III}(CN)_6]$, $M^I_2Co^{II}[Fe^{II}(CN)_6]$, $M^I_2Co^{II}_3[Fe^{II}(CN)_6]_2$, and $Co^{II}_3[Fe^{III}(CN)_6]_2$ species have been implicated in this body of work.[4,11−14] On the other hand, the combination of cyclic voltammetry, IR spectroelectrochemistry, and XPS, as employed in this study, reveals a rich vein of at least seven CoHCF species as illustrated in Table 1 and in the scheme in Figure 1. This scheme was synthesized by combining all the data presented below; it is shown at the outset as an aid to understanding the rather complex inter-relationships that exist in this system.

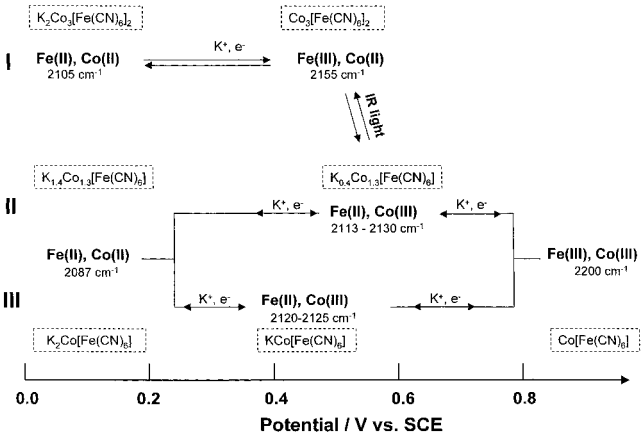

Figure 1. Schematic summary of the various compounds and their redox relationships in the CoHCF system. Three Paths I, II, III are discussed in the text.

Voltammetry of CoHCF in KNO_3 Electrolyte. Figure 2 contains voltammograms acquired during CoHCF film growth per the three procedures outlined in the Experimental section in the three frames correspondingly labeled a, b, and c. Note that the current scales in these three sets of voltammograms are different. Thus the first cycle for the combined coagulation-electrochemical film growth (method b) shows a much higher current than those corresponding to thin film growth (cf., Figure 2, parts a and b). The final profile after 30 potentiodynamic cycles showed a growth charge of ~ 20 mC cm^{-2} corresponding to a film loading of 2.1×10^{-7} mol/cm^2. This value is to be compared to the 5.2×10^{-8} mol/cm^2 attained in the a growth mode (see above). In what follows, these two nominal film loadings are referred to as "thick" and "thin" films, respectively. The c growth mode also leads to thick CoHCF films on the Au surface and the film growth is steady in this case (Figure 2c).

One noteworthy aspect of these voltammetry data is that although two main redox waves can be discerned in all the three cases, the relative prominence of the two sets of curves clearly depends on the growth mode. The voltammograms obtained (at 50 mV s^{-1}) after transferring any of these films to a pristine 1 M KNO_3 medium (after thorough washing) are practically the same as that recorded on the last growth cycle. On the other hand, decrease of the potential scan-rate (to the 1−5 mV s^{-1} range) induces splitting of the first redox wave into two components as exemplified by the scan presented in Figure 5b below for a thin film. Thus, *three* major redox processes appear to be involved in the 0−0.95 V potential range (see below).

IR Spectroelectrochemistry of CoHCF Thin Films (Loading $< 6 \times 10^{-8}$ mol/cm^2). Figure 3 shows in situ infrared spectra of a thin CoHCF film in 1M KNO_3 for the cyanide stretching spectral region. Spectra were taken at fixed potentials varied stepwise in positive (Figure 3a) and negative (Figure 3b) directions between 0.0 and 0.90 V. Voltammetric profiles for this type of film are shown in Figure 2a during its growth and in Figure 5b for its response to a slow linear potential sweep.

For spectra taken at potentials in the positive excursion, a band at 2105 cm^{-1} with a shoulder at $\sim$2087 cm^{-1} can be observed at 0.0 and 0.2 V. The shift in potential from 0.4 to 0.5 V is attended by a change in band frequency from 2105 to 2148 cm^{-1} indicating a transformation of species on the surface. Another signal at intermediate frequency, ca. 2125−2130 cm^{-1}, shows up at 0.5 V. The potential range between 0.6 and 0.9 V exhibits the absorption band at 2155 cm^{-1} accompanied by a new, weaker signature at 2200 cm^{-1} for the spectra taken at 0.8 and 0.9 V.

As the potential was progressively taken to negative values, a quasi-similar set of bands were seen, their details being slightly different from those observed on the positive potential excursion (Figure 3b). The spectrum at 0.8 V shows bands at 2155 and 2200 cm^{-1}, whereas the spectrum at 0.7 V retains only the absorption at 2155 cm^{-1} with a higher intensity than that at 0.8 V. The response at 0.6 V is the same as that at 0.7 V. The onset of the electroreduction process is detected at 0.5 V through a small shift, 2152 cm^{-1} instead of 2155 cm^{-1}, and the presence of a shoulder at ca. 2125 cm^{-1}. An interesting feature of this set of spectra is the behavior at 0.4 V where a clear band is detected at 2125 cm^{-1} with a shoulder at 2105 cm^{-1}. Reduced species with absorption at 2105 and 2087 cm^{-1} are seen to reappear in the range from 0.2 to 0.0 V. The interplay between the bands at 2105 and 2155 cm^{-1} is the main characteristic of this spectral data set.

The band areas are plotted as a function of potential after deconvolution (Figure 4). The inset in Figure 4 exemplifies the deconvolution procedure and the total spectrum profile resulting from the summation of the deconvoluted peaks. To a good approximation, peak area−potential plots show reversible behavior with slight deviations between positive and negative potential directions (compare Figure 3a with 3b, and Figure 4a with 4b).

The main features of Figures 3 and 4, therefore, are as follows:

−A steady decline of the 2105 cm^{-1} band intensity as the potential is made more positive from 0.0 V up to ca. 0.7 V, attended by a steep increase in the intensity of the 2155 cm^{-1} band from ca. 0.3 V up to 0.55 V, where it levels off.

−A steady growth from 0.0 V is observed for the 2125 cm^{-1} band intensity up to ca. 0.45 V, where after a small oscillation in magnitude, the intensity dips down slightly with potential. For potentials in the negative direction (Figure 4b), this band is still present even at 0.0 V.

−The 2087 cm^{-1} band does not follow a well-defined pattern although a drop in intensity is clearly seen between 0.4 and 0.5 V.

−The intensity, initially weak, of the 2200 cm^{-1} band starts becoming appreciable from 0.8 V.

The spectroelectrochemistry of thin films was also performed under an 11 Hz potential square wave, the amplitude set between a "sitting" potential of 0.2 V and selected upper limits up to 0.9 V (Figure 5a). A cyclic voltammogram at 5 mV s^{-1} is presented in Figure 5b to assist in the correlation between the current peaks and the corresponding infrared bands in each potential window. The infrared spectra show two bands pointing upward at $\sim$2070 and 2098 cm^{-1} that correspond to absorption at 0.2 V, their definition being mproved as the upper end of the modulation is made more positive. For 0.4 and 0.5 V as the upper limits, an infrared band pointing downward is seen at 2120 cm^{-1}. This absorption correlates with the first voltammetric process that shows up as a shoulder at ca. 0.43 V in the positive scan and as a peak at 0.3 V in the reverse scan. On the other hand, the 2155 cm^{-1} band appears from 0.6 V indicating its association with the main redox process with peaks on the voltammogram at 0.51 V and at 0.44 V for the positive- and negative-going scans, respectively. The band at 2200 cm^{-1} starts at 0.8 V associated with the voltammetric peak pair at 0.7 V. The IR absorbance at 2200 cm^{-1} seems to parallel a slight fall in intensity of the 2120 cm^{-1} signature.

Infrared Spectra of CoHCF Thick Films (Loading in the $2.0-2.5 \times 10^{-7}$ mol/cm^2 Range). Infrared spectra for thick films, whether prepared by the chemical (coagulation) or

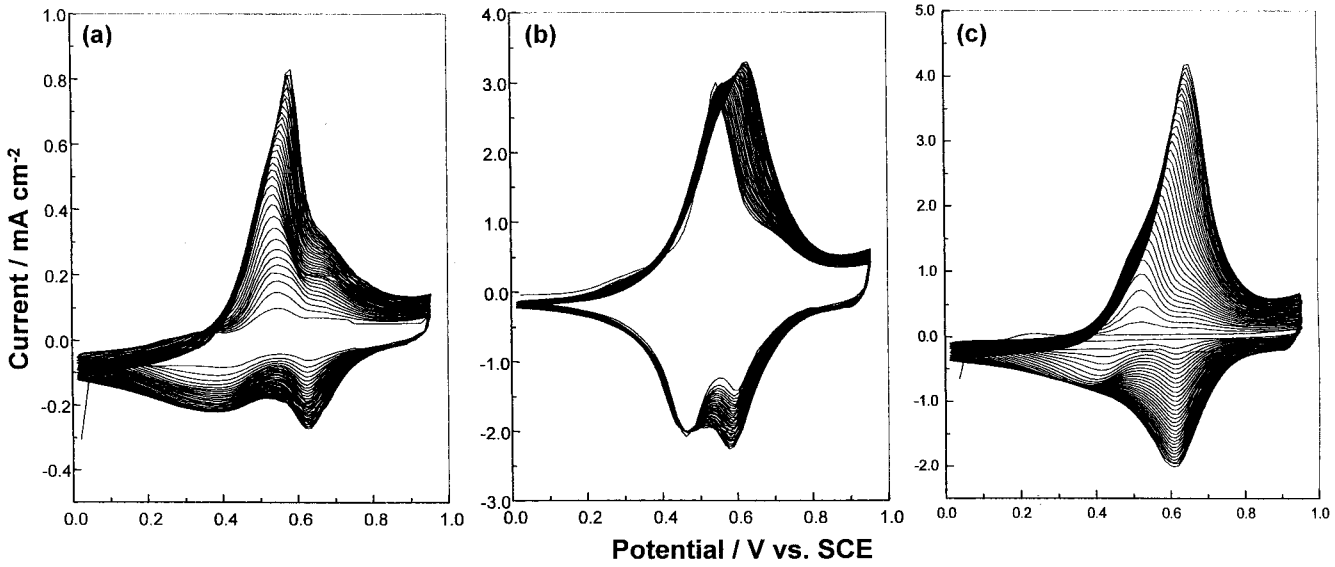

Figure 2. Repetitive cyclic voltammograms recorded during the growth of CoHCF films on gold substrates using 1×10^{-3}M $K_3[Fe(CN)_6] + 1 \times 10^{-3}$M $Co(NO_3)_2$ mixed in deoxigenated 1M KNO_3. 30 cycles at 50 mV s^{-1}. (a) electro-chemical thin film ($\delta = 80$ nm) on nonprotected gold, (b) chemical thick film ($\delta = 320$ nm) (20 min at open circuit in precursor solution), (c) electro-chemical thick film ($\delta = 335$ nm) on protected gold.

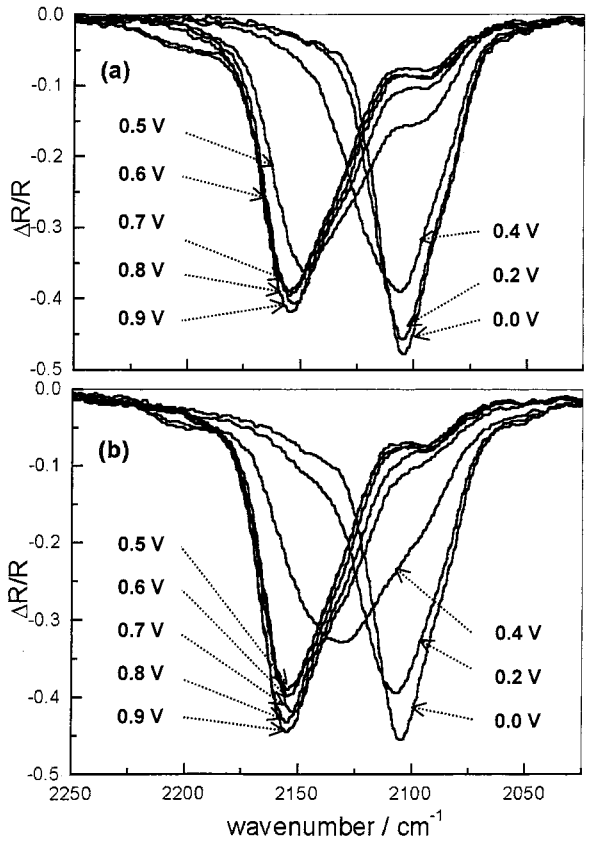

Figure 3. In situ infrared reflectance spectra of a thin CoHCF film at stepwise increasing potentials (0.0, 0.2, 0.4, 0.5, 0.6, 0.7, 0.8, 0.9 V) (a), and at the same potentials in a decreasing direction (b). Electrolyte: 1 M KNO_3. Film thickness, $\delta = 80$ nm.

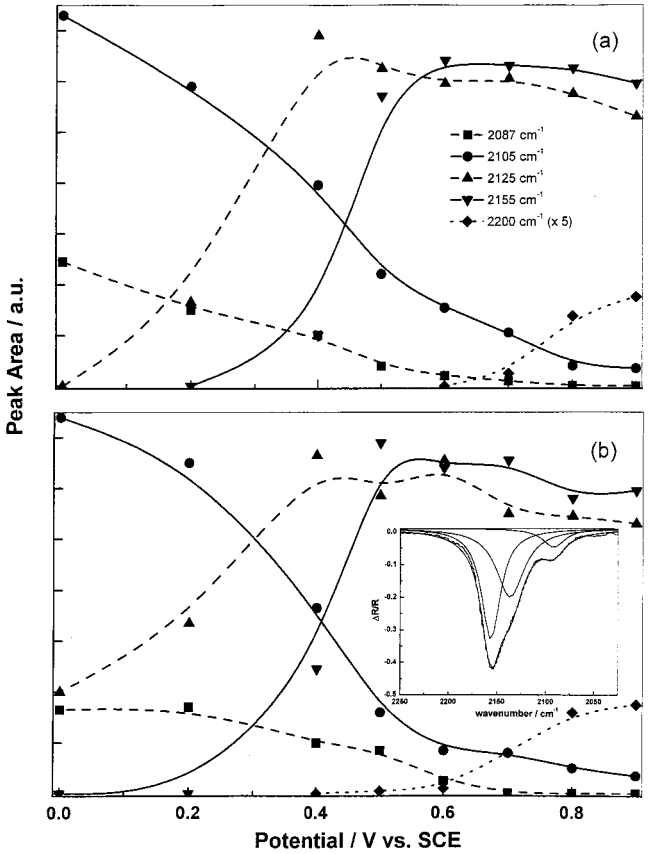

Figure 4. Peak areas of deconvoluted infrared bands as a function of potential from the spectra in Figure 2. Insert: Deconvolution of the spectrum taken at 0.7 V.

electrochemical procedure (methods b and c above), are more complex than those of the thin films. A representative set of spectra acquired in situ for a chemical CoHCF thick film (see growth voltammogram in Figure 2b) is shown in Figure 6a, where the steady-state potential is increased stepwise from 0.0 to 0.9 V and then decreased back to 0.0 V (Figure 6 b). In the 0.0−0.4 V potential range, there are two bands at 2087 and 2105 cm^{-1}. A new profile brought about by oxidation starts from 0.5 V and is made up of two main features, a dominant band that shifts with potential and other less important at ca. 2156 cm^{-1} that is observed at every potential up to 0.9 V. The dominant band is a broad feature that shifts linearly from ~2113 cm^{-1} to 2130 cm^{-1} with increasing positive potentials (Figure 7a). Absorption at 2105 cm^{-1} decreases as the potential is made more positive but is still present at 0.9 V indicating an incomplete conversion. The band at 2200 cm^{-1} is detected at

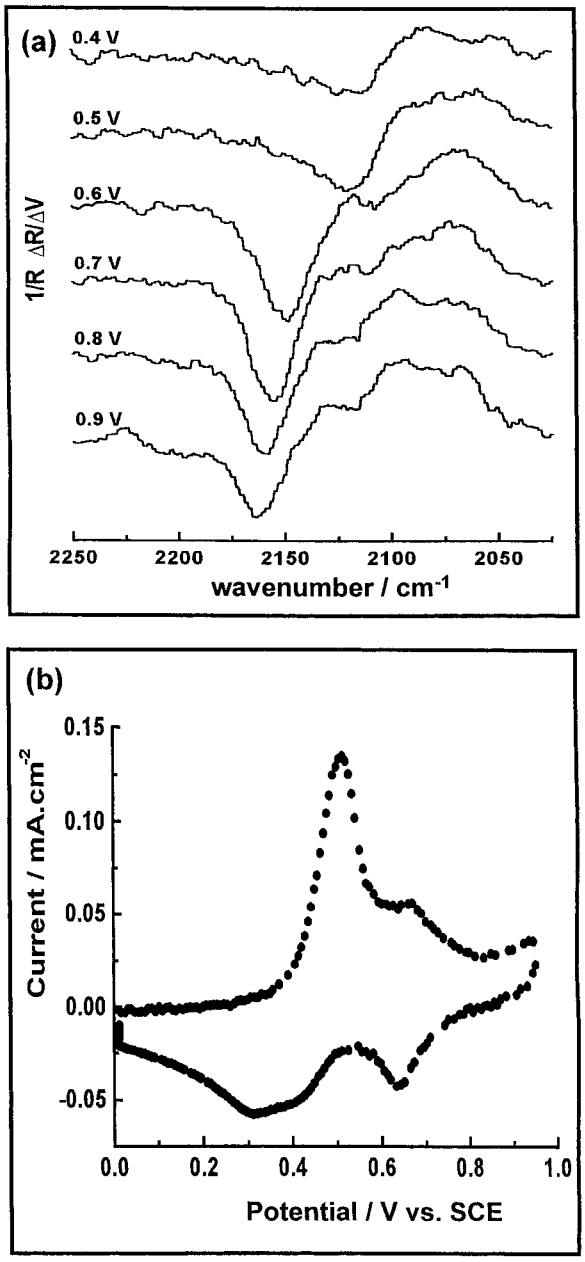

Figure 5. (a) In situ differential infrared spectra of a CoHCF film/1M KNO_3 electrolyte subjected to a 11 Hz potential modulation between the 0.2 V, and a set of variable upper limits up to 0.9 V, $\delta = 90$ nm. (b) Corresponding cyclic voltammogram at 5 mV s^{-1} in 1 M KNO_3.

0.8 and 0.9 V, its intensity paralleling a slight decrease of the 2113-2130 cm^{-1} broad feature. Some irreversibility in the spectral response is detected between positive and negative potential directions (cf., Figure 6, parts a vs b).

Band areas, corresponding to Figure 6a, are presented after deconvolution as a function of potential in Figure 7b. The dominant band moving in the 2113 cm^{-1}-2130 cm^{-1} frequency domain, *is present throughout the potential excursion*, its intensity increasing from 0.2 to 0.65 V with an arrest in the 0.4 V-0.5 V range. The 2087 cm^{-1} intensity is seen to decrease paralleling the 2113−2130 cm^{-1} band. The 2105 cm^{-1} band is not seen to disappear even at the most positive potentials where its intensity is observed to fall to ca. 40% of its value at 0.0 V. As for the other bands, the 2156 cm^{-1} intensity shows a steep increase from 0.4 to 0.55 V and then goes through a maximum. At the upper potentials, the 2200 cm^{-1} band is clearly seen from 0.7 V onward.

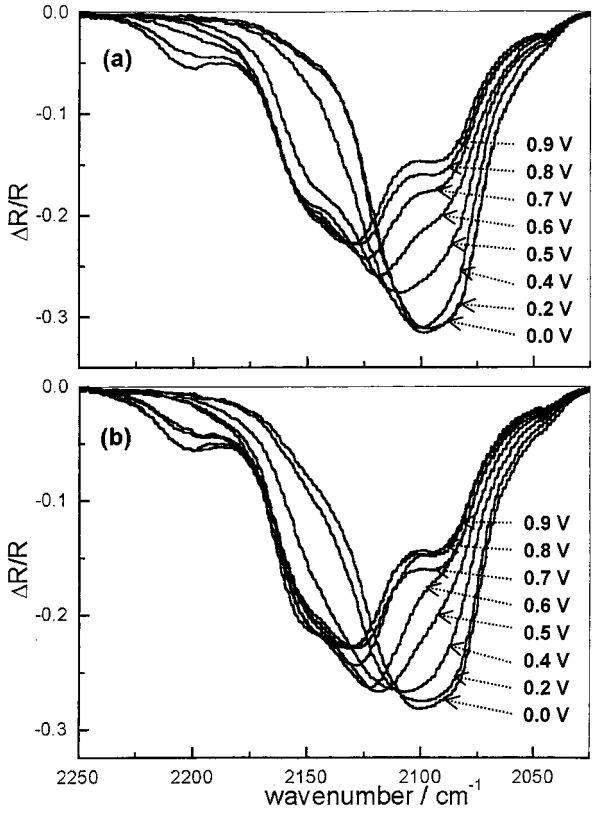

Figure 6. In situ infrared reflectance spectra of a CoHCF chemical thick film at stepwise increasing potentials (0.0, 0.2, 0.4, 0.5, 0.6, 0.7, 0.8, 0.9 V) (a), and at same potentials in a decreasing direction (b). Electrolyte: 1 M KNO_3, $\delta = 320$ nm.

Thin Films vs Thick Films. Thin films (Figures 3-5) exhibit marked differences in their infrared spectra when compared with thick layers (Figures 6, 7). The absorption at 2087 cm^{-1} and ca. 2130 cm^{-1} are more prominent in thick coatings whereas the band at 2155 cm^{-1}, clearly resolved in thin layers, is present just as a shoulder in chemical thick films. Other bands are, on the whole, common to both preparations/film loadings.

A comparison of the infrared behavior of thin versus thick films is presented in Figure 8 for the three preparation protocols. These data were processed as reflectance difference spectra using as reference the spectrum obtained at 0.0 V, and have bipolar profiles with up-going bands arising from species disappearing at 0.0 V, and down-going bands stemming from absorption at positive potentials, that is, from 0.2 to 1.0 V.

For the thin film (Figure 8a), the bipolar bands increase in intensity as the potential is made more positive. The band at 2105 cm^{-1} in the reduced state and 2155 cm^{-1} after oxidation at the positive limit are the dominant features, whereas a positive shoulder at 2087 cm^{-1} seems to be linked to a sideband at ca. 2125 cm^{-1} in the oxidized state. This last pair is clearly observed throughout the potential range. A weak band at 2200 cm^{-1} is seen from 0.8 V onward.

More complex band interplay is observed for the thick films (Figure 8, parts b and c). The chemically prepared film of Figure 8b shows the partnership of two sets of bands, 2087 cm^{-1}/2113−2130 and 2105 cm^{-1}/2155 cm^{-1}. The 2200 cm^{-1} signature is more clearly observed in thick films than in thin ones. The 2113−2130 cm^{-1} absorption was found to increase in intensity and shifts to higher wavenumbers with potential. The electrochemical thick film (Figure 8c) shows only the partnership of one set of bipolar bands at 2120−2130 cm^{-1} and 2087 cm^{-1}

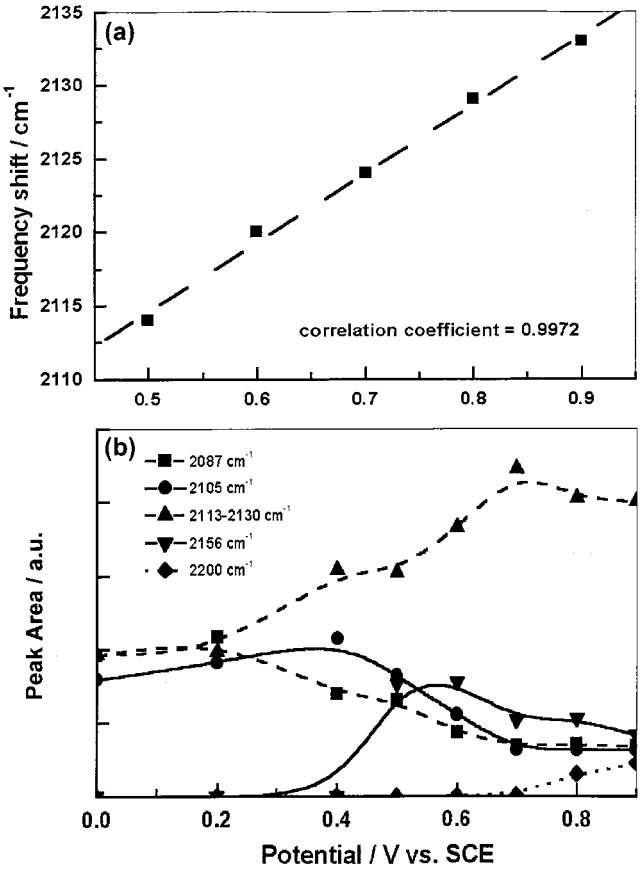

Figure 7. (a) Frequency shift vs potential for the broad dominant band peaking in the 2113−2130 cm^{-1} range. (b) Peak areas of deconvoluted infrared bands as a function of potential (data from the spectra in Figure 6a.)

respectively. The 2200 cm^{-1} band only appears at the most positive potentials.

Effect of Foreign Cations (Na^+, K^+, and Rb^+) on the CoHCF Infrared Spectra. Figure 9 shows infrared spectra of coagulated CoHCF precipitates formed according to the preparative protocol b (cf., Figure 2b) except for the use of 0.1 M MNO_3 (M = Na, K, or Rb) solutions instead of 1 M KNO_3 as in Figure 2b. The choice of 0.1 M MNO_3 solutions is due to the low solubility of the rubidium salt that precludes the preparation of 1 M solutions. The spectra in Figure 9 exhibit three main bands at ∼2156 cm^{-1}, 2120−2125 cm^{-1}, and 2088 cm^{-1}. The predominance of one band over the others depends on the foreign cation whereas their frequencies are not affected.

Table 1 also lists the IR-active bands, $\nu_6(F_{1u})$, of Fe−CN−Co bridge entities reported in the literature.[5,7,19−22] The CN stretching frequencies depend on the Co and Fe oxidation state, the higher the oxidation state, the stronger the σ bonding of C−Fe and N−Co and, consequently, the higher the $\nu_6(F_{1u})$ frequency. Stretching vibrations are in the 2085−2105 cm^{-1} range for a cyanide bridging Fe(II) and Co(II), whereas the range 2115−2165 cm^{-1} includes the cyanide bridging Fe(III) and Co(II), and Fe(II) and Co(III). Finally, stretching frequencies for a cyanide between Fe(III) and Co(III) are reported to fall in the 2190-2200 cm^{-1} range.[22] The sharp band at 2156 cm^{-1}, that is dominant in a sodium environment, is assigned to a cyanide stretching vibration mode in a [Fe(III),Co(II)] configuration with a Co/Fe ratio of 1.5.

Going from Na^+ to K^+ and Rb^+, the 2156 cm^{-1} band [cyanide bridging Fe(III) and Co(II)] decreases markedly and leads to the predominance of the 2120−2125 cm^{-1} band [Fe(II) and Co(III)] (see Figure 9 and Table 1). Interestingly, the structure providing the 2088 cm^{-1} band [species containing Fe(II) and Co(II)] appears better resolved in sodium electrolytes than in the other two solutions, and seems to be generated during the negative-going potential scans.

In CoHCF compounds containing rubidium, the predominant band lying at 2120−2125 cm^{-1} points to the dominance of a structure containing mainly Fe(II) and Co(III) entities, that is with a Co/Fe ratio of 1.3 and a M/Fe ratio of 0.4. In contrast, this is the weakest band observed in sodium electrolytes. At an intermediate situation, the compound that coagulates in K^+ electrolytes resembles more of the compound with Rb^+ than that with Na^+. For potassium electrolytes with increased concentration from 0.1 to 1 M (spectrum not shown), other conditions being the same, the band at 2120−2125 cm^{-1} intensifies and that at 2156 cm^{-1} weakens leading to a strong similarity with the spectrum (c) obtained in the presence of rubidium cations. No band at 2200 cm^{-1}, that is associated with a structure containing Fe(III) and Co(III), was detected in any of these coagulated compounds (Figure 9).

XPS Surface Analysis of CoHCF Films. Determination of Co/Fe, K/Fe, and K/Co element ratios for CoHCF films was carried out by ex situ XPS surface analysis. Table 2 contains the XPS assays of representative CoHCF films prepared on gold foils. The element ratios were obtained from the integration of the corresponding high-resolution XP spectra for the entire 2p binding energy region of each element. Table 2 also provides film charges (as well as corresponding loadings in mol/cm^2) and average stoichiometries as derived from the element ratios.

The XPS analysis on its own cannot discern how many different stoichiometries are present in the films. However, with the aid of the infrared spectroelectrochemical data presented above, a comprehensive description of the film composition as a function of potential, can be assembled. XPS assays provide the following trends in composition as influenced by the film thickness and preparation protocols:

(a) All of the films disconnected at the negative potential limit show only XPS signals for Fe(II).

(b) Co/Fe ratio are in the 1.1−1.4 range. The highest Co/Fe ratio (1.4) was found for the thick coagulated films (e.g., from method 'b').

(c) Thin films were found to contain a higher amount of potassium than thick films. Compare the K/Fe and K/Co ratios for Film I with those for Films II through IV.

(d) The amount of potassium in the film depends on potential. Film IV is depleted of potassium because it was disconnected at 0.95 V.

In the last column of Table 2, some possible stoichiometries are provided for the film composition. For Film I, two structures are postulated with the assistance of the infrared spectra of the corresponding films (Figs. 3, 4 and Table 1). For the rest of the films, only average compositions were estimated from the element ratios reported. It is worth noting that some of these formulas cannot afford electroneutrality without considering the presence of Co(III) in the structure (for instance, Films III and IV).

A comparison of high-resolution XPS data for the Fe and Co signals is shown in Figure 10 for an electrochemical thick CoHCF film disconnected at the lower, 0.0 V (Figure 10 A1, A2), and upper, 0.95 V, potential limits (Figure 10 B1, B2). It is noteworthy that for the reduced film, the Fe spectrum shows the Fe_{2p1} and Fe_{2p3} peaks at 721.2 and 708.4 eV, respectively (Figure 10 A1), whereas for the Co spectrum, three peaks show up; a Co_{2p1} peak at 797.8 eV and two overlapped Co_{2p3} peaks

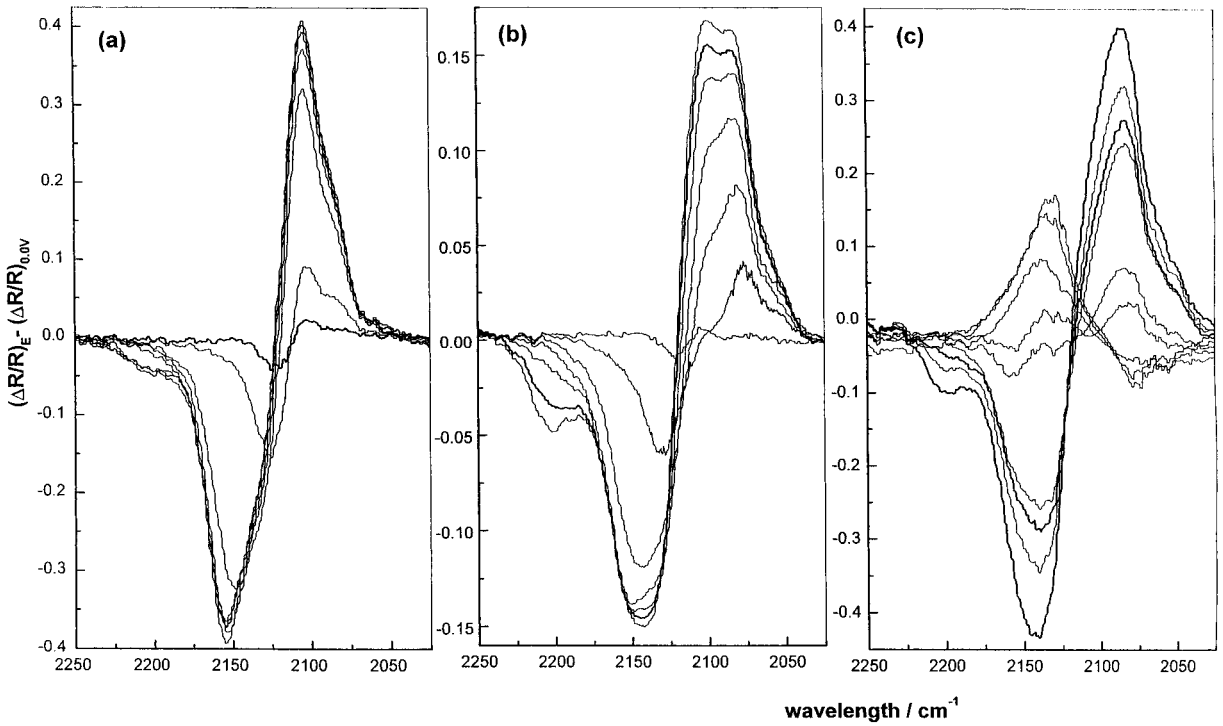

Figure 8. Infrared difference reflectance spectra of CoHCF thin and thick films in 1 M KNO_3. (a) electrochemical thin film (δ = 80 nm), (b) chemical thick film (δ = 320 nm) and (c) electrochemically thick film on protected gold (δ = 335 nm).

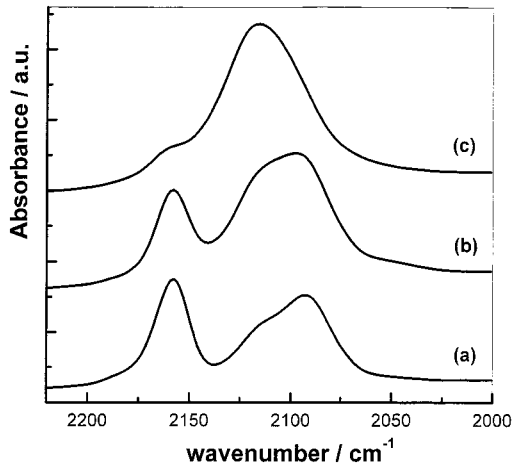

Figure 9. Infrared spectra of precipitates obtained from electrochemical preparation of chemical thick films using 10^{-3} M $Co(NO_3)_2$ + 10^{-3} M $K_3Fe(CN)_6$ + 0.1 M MNO_3 with M = Na (a), K (b), and Rb (c).

at 782.7 and 781.2 eV, respectively (Figure 10 A2). The corresponding spectral regions for the oxidized film are shown in Figure 10 B1, B2. The Fe region shows two sets of peaks for Fe_{2p1} and another set of two for Fe_{2p3} contrasting with the spectrum of the reduced film. These new peaks (Figure 10 B1) clearly confirm the presence of Fe(III) in the film. Interestingly, Fe(II) signals are also present in oxidized films.

With respect to the Co spectral region (Figure 10 B2), there are no clear-cut changes comparable to those shown for the Fe region: the Co_{2p3} region shows two main peaks and a shoulder that have binding energy shifts of 15.10 and 16.20 eV, respectively. Both Co_{2p1} and Co_{2p3} peaks are broader upon oxidation and show small satellite peaks at their higher energy side (marked with*). It is worth mentioning that Co(III) electrochemically formed on oxidized cobalt electrodes have a Co_{2p1} peak at 798.4 eV and a $Co_{2p2/3}$ at 782.4 eV, with a binding energy shift of 16.1 eV.[26]

Photochemical Activation of CoHCF Redox Sites. Figure 11 shows the evolution of two sets of voltammograms, under continuous infrared irradiation (Figure 11a) and in the subsequent dark periods (Figure 11b). A series of voltammograms were recorded at selected times during irradiation with wavelengths longer than 675 nm as obtained from a 100 W tungsten−halogen lamp and a suitable cutoff filter. Irradiation was performed at open-circuit for pre-selected lapses of time, the potential scan being started from the open circuit potential in the positive direction before completing the potential cycle. With an increase of irradiation time, the voltammograms show a systematic and reversible current increase along with a negative shift of the main voltammetric peaks. After ca. 25 min of irradiation, the voltammetric profiles attain a stationary state. Once this stationary condition is achieved, light interruption at open circuit brings about a spontaneous return to the initial, nonirradiated, condition in a time lapse slightly longer than that for the transformation under IR light (Figure 11b). The film photoactivation instigates an increase in the number of electrochemically active entities (charge increases). The corresponding evolution and its return in the dark to the initial condition are presented in Figure 12. This procedure can be reversibly repeated (not shown).

General Discussion

Dark Redox Processes. The IR spectroelectrochemistry and XPS data presented in the preceding section underline a degree of complexity in the CoHCF system, that do not appear to have been recognized by previous authors in electrochemical studies.[4,11−14] Interestingly, cyclic voltammograms essentially similar to those presented in Figure 2, have also been reported by previous authors but interpreted in terms of only 2−4 CoHCF species (see above).

The scheme in Figure 1, synthesized from considering all our data as a unit, clearly indicates that the CoHCF system is considerably more complex. The potential (energy) domains of existence of the various species, culled from the IR spectral

TABLE 2: Surface Analysis of the Three Types of CoHCF Films (see Experimental Section) by X-ray Photoelectron Spectroscopy

type of film	charge and film loading	Co/Fe[d]	K/Fe[d]	K/Co[d]	average stoichiometry
(I) thin film[a]	$Q = 6.2$ mC/cm^2 $\Gamma = 6.4 \times 10^{-8}$ mol/cm^2 [c]	1.1	1.7	1.2	$K_2Co[Fe(CN)_6]$ (70−80%) $K_2Co_3[Fe(CN)_6]_2$ (20−30%)
(II) chemical thick film[a]	$Q = 25.3$ mC/cm^2 $\Gamma = 4.1 \times 10^{-7}$ mol/cm^2 [c]	1.4	1.1	0.9	$K_{1.2}Co_{1.4}[Fe(CN)_6]$
(III) electrochemical thick film[a]	$Q = 22.1$ mC/cm^2 $\Gamma = 3.4 \times 10^{-7}$ mol/cm^2 [c]	1.2	0.6	0.6	$K_{0.7}Co_{1.1}[Fe(CN)_6]$
(IV) electrochemical thick film[b]	$Q = 20.9$ mC/cm^2 $\Gamma = 2.1 \times 10^{-7}$ mol/cm^2 [c]	1.1	0.3	0.4	$K_{0.2}Co_{1.1}[Fe(CN)_6]$ $K_{0.4}Co_{1.2}[Fe(CN)_6]$

[a] Electrode disconnected at 0.0 V. [b] Electrode disconnected at 0.95 V. [c] Γ = film loading (CoHCF surface concentration). [d] Nominal uncertainty: ± 0.1.

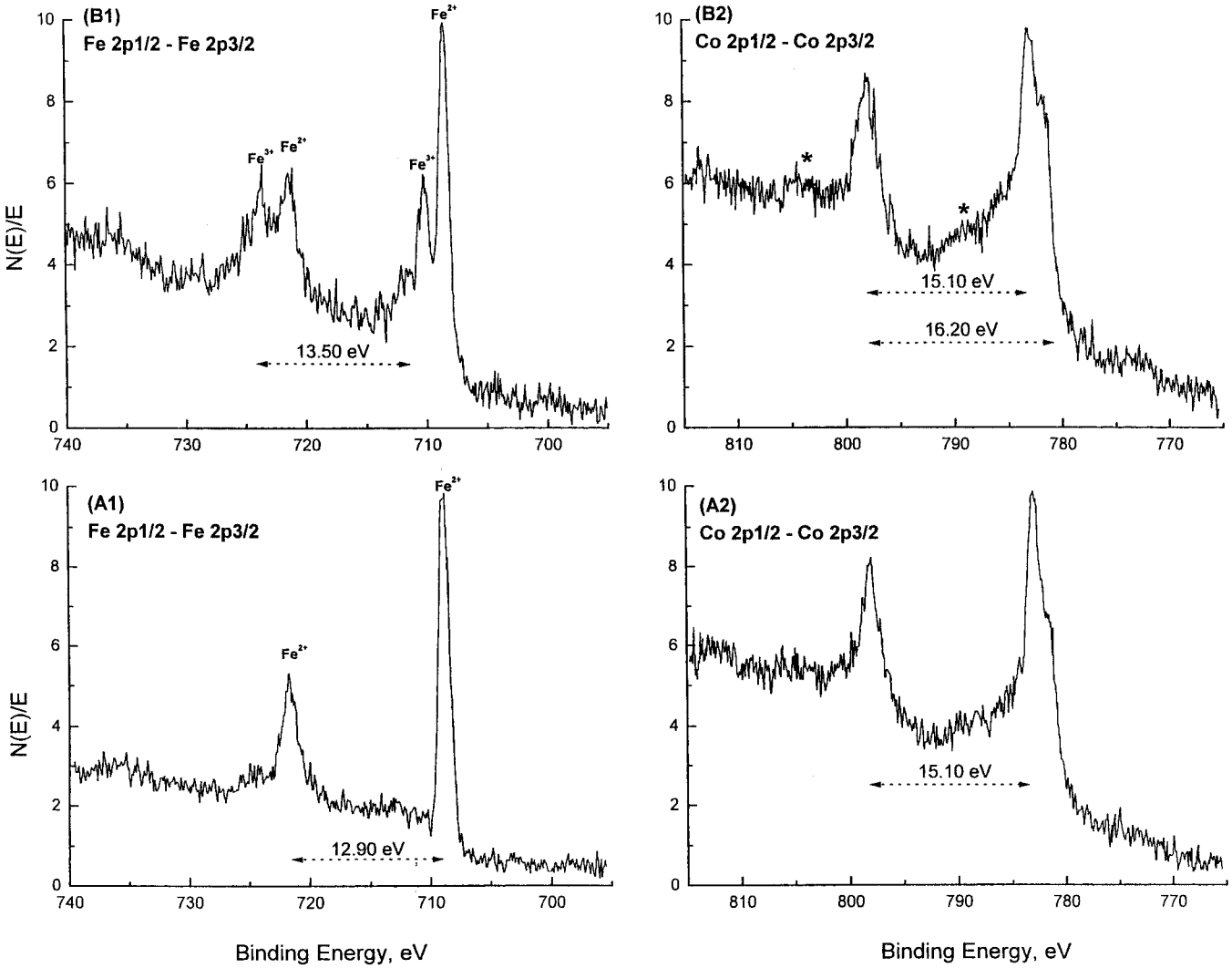

Figure 10. High-resolution Fe_{2p} and Co_{2p} XPS data on CoHCF films prepared on gold foil under protected conditions. Potentiostat switched off at 0.0 V (A), and at 0.95 V (B), after 30 cycles in 10^{-3} M $Co(NO)_3$ + 10^{-3} M $K_3[Fe(CN)_6]$ + 1.0 M KNO_3.

data, are also shown in this scheme. Three processes labeled I, II, and III are postulated as electrochemically independent, and two of them become linked through the photoinduced transfer (Figures 11 and 12).

Path I is a confined redox process involving the [Fe(III),Co(II)]/[Fe(II),Co(II)] species in the $Co^{II}_3[Fe^{III}(CN)_6]_2$ structure, that converts to the corresponding $K_2Co^{II}_3[Fe^{II}(CN)_6]_2$ counterpart. The general equation for this process can be written as

$$Co^{II}_3[Fe^{III}(CN)_6]_2 + 2e^- + 2K^+ \leftrightarrow K_2Co^{II}_3[Fe^{II}(CN)_6]_2 \quad (1)$$

The electrochemical conversion between these two entities was clearly tracked by their in situ infrared characteristic frequencies at 2155 cm^{-1} for $Co_3[Fe(CN)_6]_2$ and 2105 cm^{-1} for $K_2Co^{II}_3[Fe^{II}(CN)_6]_2$ (Figures 3−5 and Table 1). The rate of interconversion is dictated by the uptake/release of potassium cations during the reduction/oxidation process. As the $Co^{II}_3[Fe^{III}(CN)_6]_2$ structures have all the tetrahedral interstices empty, the uptake of potassium should not present difficulties and a quasi-reversible, kinetically fast behavior is observed in the evolution of the two infrared bands (see differential spectra at 11 Hz in Figure 5), with a redox potential for this couple centered at ca. 0.45−0.50 V (as obtained from Figure 4).

Thin films show another pair of IR bands located at ca. 2125 cm^{-1} and at 2087 cm^{-1}. They are attributed to Path III in Figure 1. Path III takes place at more negative potentials than the

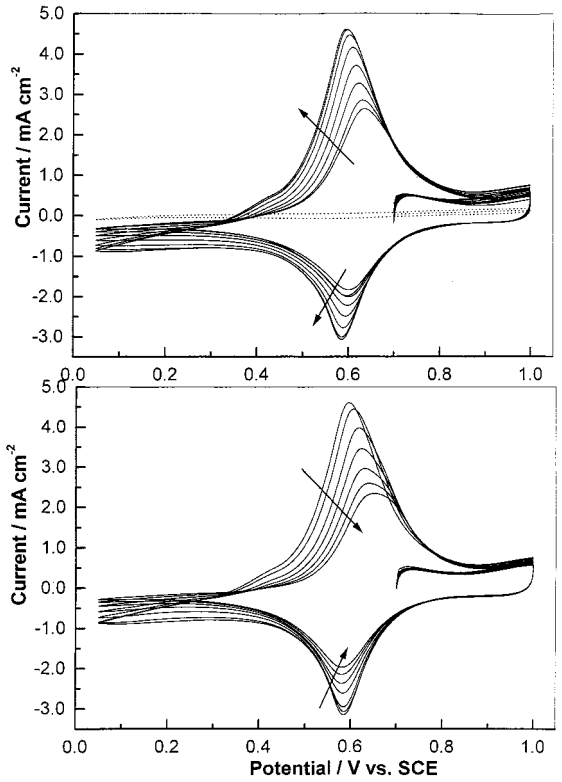

Figure 11. (a) Voltammograms for a CoHCF film in 1 M KNO_3 as a function of irradiation time. Illumination from a quartz halogen lamp (wavelengths longer than 675 nm, 2.1 mW/cm^2), for time t = 0, 1, 3, 5, 8, 11, 15, 18, 24 min. (b) Post-irradiation relaxation (at open circuit) to the initial state (t = 0, 3, 6, 9, 12,15, 18, 22 min in the dark). Voltammograms started from open circuit potential. Scan rate = 50 mV s^{-1}. A voltammogram for Au in 1 M KNO_3 is also shown in Figure 11 a (- - -).

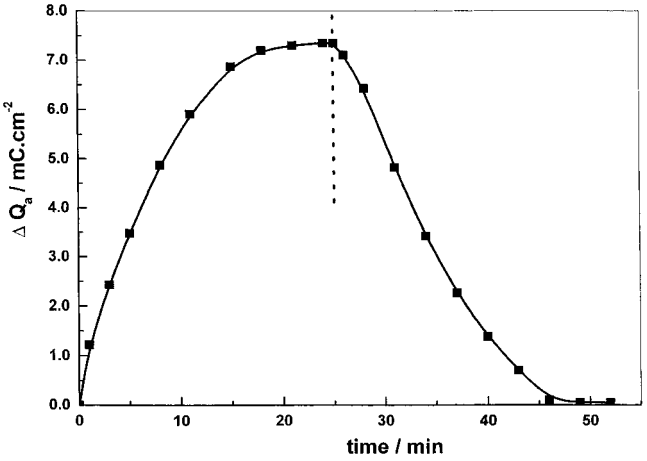

Figure 12. Plot of ΔQ_a as a function of irradiation time (up to the dot vertical line) and during dark time period (passing the dot line). ΔQ_a is equal to $Q_a^t - Q_a^{t=0}$, with Q_a^t being the voltammetric charge at a pre-selected irradiation time and $Q_a^{t=0}$ the corresponding charge before starting the irradiation for the ascending branch. For the descending branch, $\Delta Q_a = Q_a^{t+t_d} - Q_a^{t=0}$, with $Q_a^{t+t_d}$ being the charge in dark after shutting off the light.

process corresponding to the 2155 cm^{-1}/2105 cm^{-1} redox set (see Figures 3 and 4). With the aid of the infrared frequencies listed in Table 1, the broad 2125 cm^{-1} band can be assigned to the $KCo^{III}[Fe^{II}(CN)_6]$ structure. Consequently, the electrochemical process can be written as

$$KCo^{III}[Fe^{II}(CN)_6] + e^- + K^+ \leftrightarrow K_2Co^{II}[Fe^{II}(CN)_6] \quad (2)$$

This transformation, observed through the 2125 cm^{-1}/2087 cm^{-1} bands, is also reversible in thin films, as indicated by its ability to follow the 11 Hz potential modulation (Figure 5). The process requires potassium cations being rapidly inserted in the semi-empty tetrahedral sites (with $^1/_4$ of them are already occupied). The insertion of potassium concomitant with film electroreduction is borne out by quantitative XPS assays showing an average K/Fe ratio of 1.7 ± 0.1 (Table 2). This result points to the K_2-$Co[Fe(CN)_6]$ structure (eq 2) as the main component in reduced thin films. This reduced structure manifests through the 2087 cm^{-1} band in the corresponding infrared spectra. Its contribution however is not dominant in thin film spectra, probably due to a low extinction coefficient.

The broad band at 2125 cm^{-1} is assigned to the stretching of cyanide bridging Fe(II) and Co(III) and in a CoHCF structure bearing a Co/Fe ratio of unity. In this structure, conversion from [Fe(III),Co(II)] species to the more stable [Fe(II),Co(III)] species, occurs via electron transfer from Co(II) to Fe(III) through cyanide bridges.

Path III also includes an additional electrode process leading to a more oxidized state of the film and involving the [Fe(II),-Co(III)]/[Fe(III),Co(III)] conversion. This reaction is signaled by the appearance of a weak band at 2200 cm^{-1} at potentials higher than 0.7 V (see Figures 3−5, and Table 1). The conversion is only partially completed as the 2125 cm^{-1} intensity barely decreases when the [Fe(III),Co(III)] species (at 2200 cm^{-1}) starts appearing. Paths I and III thus involve redox processes related to CoHCF structures with Co/Fe ratios of 1.5 and 1.0 respectively, both being the most common stoichiometries for CoHCF compounds. Their potential windows of stability are confirmed by cyclic voltammetry performed at slow scan rates (Figure 5b).

On the other hand, Path II in Figure 1 involves thick films that are dominated by intermediate CoHCF stoichiometries with Co/Fe ratios between 1.0 and 1.5 (Table 1). The infrared spectra of thick films significantly differ from those of thin films. For chemical (coagulated) thick films, C≡N stretching bands related to [Fe(II),Co(II)] species with frequencies of 2087 cm^{-1} and 2105 cm^{-1} are clearly seen, the 2087 cm^{-1} species converting only partially to a broad band that shifts to the 2113-2130 cm^{-1} range with the oxidation potential (Figures 6 and 7a). This shift in frequency resembles the behavior reported for species with the $K_{0.4}Co_{1.3}[Fe(CN)_6]$ formula, i.e., with a Co/Fe =1.3 stoichiometry.[5,7] Note that a band at 2120−2125 cm^{-1} is clearly present in thin films but it is not related to a Co/Fe = 1.3 but instead to a Co/Fe = 1.0 stoichiometry as shown by XPS data. In fact, thick films have a higher Co/Fe ratio than that prevailing in thin films (Table 2) pointing to a Co/Fe ≈ 1.3 stoichiometry that can be expressed through the following main electrochemical reaction

$$K_{0.4}Co^{III}{}_1Co^{II}{}_{0.3}[Fe^{II}(CN)_6] + 1e^- + K^+ \leftrightarrow K_{1.4}Co^{II}{}_{1.3}[Fe^{II}(CN)_6] \quad (3)$$

Reaction 3 involves Co(III)/Co(II) redox centers instead of Fe(III)/Fe(II) centers, the former being favored in potassium electrolytes at room temperature as reported elsewhere.[5c]

Path II also includes partial electrooxidation to [Fe(III), Co(III)] pairs, as indicated by the presence of the 2200 cm^{-1} band. This band however was not detected in precipitates formed during film preparation (Figure 9), indicating that these species are only formed by electrochemical oxidation and not via chemical reaction. In contrast, the broad 2113−2130 cm^{-1} band appears as the main contribution not only in chemical thick films

SCHEME 1: Photoinduced Transition (see Figures 11 and 12) Showing the Changes at the Fe and Co Redox Centers

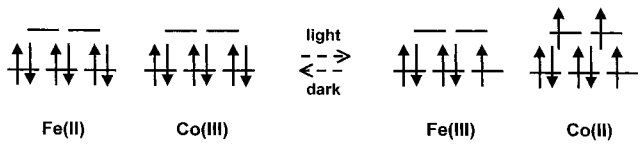

(Figures 6 and 7b) but also in the precipitates (Figure 9, spectrum b) suggesting that the coagulation on the electrode surface may be important in the formation of thick films.

In other aspects, electrochemical thick films show common features with chemical films of comparable thickness mostly in the spectral dominance of the 2113−2130 cm^{-1} band (Path II). However, Path I is clearly more discernible in chemical than in electrochemical thick films, as the former show a higher contribution of the 2156 cm^{-1} band than do electrochemical thick films (Figure 8). As these two bands (related to Paths II and I) correspond to CoHCF structures with Co/Fe = 1.5 and 1.3 respectively, the average stoichiometries of chemical films should be somewhat between these two Co/Fe ratios (XPS confirms a Co/Fe = 1.4 for this type of films). Furthermore, the XPS detection of Fe(II) in oxidized films (Figure 10) points to the existence of species with Fe(II) and Co(III) sites.

The 2200 cm^{-1} band is found in thick films with higher intensity than in thin layers. This highly oxidized species with [Fe(III), Co(III)] pairs are only present in CoHCF films that had been exposed to positive potentials. These species do not seem to arise from the oxidation of structures with [Fe(III),-Co(II)] pairs (with Co/Fe = 1.5) as inferred from the comparison between the infrared spectra of thin and thick films.

Photoactivated Redox Process. There is also a possibility that at room temperature, light-induced electron transfer from Co(III) to Fe(II), would bring about changes in the film voltammetric profile through the photoactivation of inactive redox centers. The evolution of voltammograms for an electrochemical thick film under near-IR irradiation (Figure 11) shows this phenomenon manifested as a net increase in current and redox reversibility. This process was observed to reach a saturation condition. Light interruption at open circuit after photoactivation is followed by a spontaneous return to the more stable oxidized configuration (Figure 12).

It is relevant to mention here that during photoactivation, the [Fe(II),Co(III)] pairs (photoconverted to [Fe(III),Co(II)]) undergo an elongation in the Co−N distance that results in a reported expansion of the unit cell parameter from 9.96 to 10.32 Å.[5d,27] This lattice expansion may also contribute to the increased redox reversibility of the films in that it may widen the channels through which potassium ions move as required by electroneutrality.

The photoinduced redox transformation is schematically shown to result in the conversion of low-spin Co(III) species to their high spin Co(II) counterparts (Scheme 1). The photoconverted [Fe(III), Co(II)] pairs are then more easily electroreduced on a subsequent potential scan by invoking Path I (Figure 12). The master scheme in Figure 1 shows that this photoactivated process provides the link between the oxidized species generated via Paths I and II, respectively.

Concluding Remarks

This study builds upon, and considerably extends, the previous electrochemical observations[4,11−14] of various compound stoichiometries in the CoHCF system. A comprehensive redox scheme emerges from this study based on seven distinct CoHCF species that are inter-linked through three independent pathways and charge-transfer processes in the dark and activated by IR radiation. The combination of cyclic voltammetry, IR spectroelectrochemistry, and ex situ XPS analyses of the resultant films affords a self-consistent picture of how the various compound stoichiometries are linked in this complex system.

Acknowledgment. This collaborative project was facilitated by travel funds through the NSF/CONICET International Programs between the U.S. and Argentina. K.R. and N.R. de T. acknowledge partial financial support from the U.S. Department of Energy (Office of Basic Energy Sciences). We thank a reviewer for constructive criticisms of an earlier manuscript version.

References and Notes

(1) Itaya, K.; Uchida, I.; Neff, V. D. *Acc. Chem. Res.* **1986**, *19*, 162.
(2) Monk, R. M. S.; Mortimer, R. J.; Rosseinsky, D. R. *Electrochromism: Fundamentals and Applications*; VCH: Weinheim, 1995.
(3) Granqvist, C. G. *Handbook of Electrochromic Materials*; Elsevier: Amsterdam, 1995.
(4) (a) Kulesza, P. J.; Malik, M. A., Zamponi, S.; Berrettoni, M.; Marassi, R. *J. Electroanal. Chem.* **1995**, *397*, 287. (b) Kulesza, P. J.; Malik, M. A.; Miecznikowski, K.; Wolkiewicz, A.; Zamponi, S.; Berrettoni, M.; Marassi, R. *J. Electrochem. Soc.* **1996**, *143*, L10.
(5) (a) Sato, O.; Iyoda, A.; Fujishima, A.; Hashimoto, K. *Science* **1996**, *272*, 704. (b) Sato, O.; Einaga, Y.; Iyoda, A.; Fujishima, A.; Hashimoto, K. *J. Electrochem. Soc.* **1997**, *144*, L11. (c) Sato, O.; Einaga, Y.; Iyoda, A.; Fujishima, A.; Hashimoto, K. *J. Phys. Chem. B* **1997**, *101*, 3903. (d) Sato, O.; Einaga, Y.; Fujishima, A.; Hashimoto, K. *Inorg. Chem.* **1999**, *38*, 4405.
(6) Yoshizawa, K.; Mohri, F.; Nuspl, G.; Yamabe, T. *J. Phys. Chem. B* **1998**, *102*, 5432.
(7) (a) Bleuzen, A.; Lomennech, C.; Escax, V.; Villain, F.; Varret, F.; Cartier dit Moulin, Ch.; Verdaguer, M. *J. Am. Chem. Soc.* **2000**, *122*, 6648. (b) Cartier dit Moulin, Ch.; Villain, F.; Bleuzen, A.; Arrio, M. A.; Sainctavit, Ph.; Lomenech, C.; Escax, V.; Baudelet, F.; Dartyge, E.; Gallet, J.-J.; Verdaguer, M. *J. Am. Chem. Soc.* **2000**, *122*, 6653.
(8) Green-Pederson, H.; Korshin, G. V. *Environ. Sci. Technol.* **1999**, *33*, 2633.
(9) Chen, S.-M. *Electrochim. Acta* **1998**, *43*, 3359.
(10) Cataldi, T. R. I.; de Benedetto, G.; Bianchini, A. *J. Electroanal. Chem.* **1999**, *471*, 42.
(11) (a) Cai, C.-X.; Ju, H.-X.; Chen, H.-Y. *J. Electroanal. Chem.* **1995**, *397*, 185. (b) Cai, C.-X.; Xue, K.-H.; Xu, S.-M. *J. Electroanal. Chem.* **2000**, *486*, 111.
(12) Kulesza, P. J.; Malik, M. A.; Berrettoni, M.; Giorgetti, M.; Zamponi, S.; Schmidt, R.; Marassi, R. *J. Phys. Chem.* **1998**, *102*, 1870.
(13) Joseph, J.; Gomathi, H.; Prabahakara Rao, G. *J. Electroanal. Chem.* **1991**, *304*, 263.
(14) (a) Jiang, M.; Zhou, X.; Zhao, Z. *Ber. Bunsen-Ges. Phys. Chem.* **1991**, *95*, 720. (b) Gao, Z.; Wang, G.; Li, P.; Zhao, Z. *Electrochim. Acta* **1991**, *36*, 147. (c) Gao, Z.; Bobacka, J. Ivaska, A. *Electrochim. Acta* **1993**, *38*, 379. (d) Zhang, H.-Q.; Lin, X.-Q. *Talanta* **1997**, *44*, 2069.
(15) Beden, B.; Lamy, C.; Léger, J.-M. *Modern Aspects of Electrochemistry*; Bockris, J. O'M., Conway, B. E., White, R., Eds.; Plenum Press: New York, 1992; Vol. 22, p 97.
(16) (a) Lezna, R. O.; Kunimatsu, K.; Ohtsuka, T.; Sato, N. *J. Electrochem. Soc.* **1987**, *134*, 3090. (b) Lezna, R. O. *An. Asoc. Quím. Argent.* **1994**, *82*, 293.
(17) de Tacconi, N. R.; Rajeshwar, K.; Lezna, R. O. *J. Phys. Chem.* **1996**, *100*, 18234.
(18) Inoue, H.; Fluck, E. *Z. Naturforsch.* **1983**, *386*, 687.
(19) Ayers, J. B.; Waggoner, W. H. *J. Inorg. Nucl. Chem.* **1971**, *33*, 721.
(20) Ghosh, S. N. *J. Inorg. Nucl. Chem.* **1974**, *36*, 2465.
(21) Hester, R. E.; Nour, E. M. *J. Chem. Soc., Dalton Trans.* **1981**, 938.
(22) Reguera, E.; Bertran, J. F.; Diaz, C.; Blanco, J. *Hyperfine Interac.* **1990**, *53*, 391.
(23) Mallat, T.; Thiebaut, S.; Verdaguer, M.; Veillet, P. *Science* **1993**, *262*, 1554.
(24) Ludi, A.; Gudel, H. U. *Structure and Bonding*; Springer-Verlag: Berlin, 1973; p. 1.
(25) Griebler, W.-D.; Babel, D. *Z. Naturforsch.* **1982**, *37b*, 832.
(26) Ismail, K. M.; Badawy, W. A. *J. Appl. Electrochem.* **2000**, *30*, 1303.
(27) Gallois, B.; Real, J. A.; Hauw, C.; Zarembowitch. J.*Inorg. Chem.* **1990**, *29*, 1152.